


Broadband Labyrinthine Acoustic Insulator

Ao Chen,^{1,2,‡} Xiaoguang Zhao,^{2,3,‡} Zhiwei Yang,^{1,2} Stephan Anderson,^{2,3,*} and Xin Zhang^{1,2,†}

¹*Department of Mechanical Engineering, Boston University, Boston, Massachusetts 02215, USA*

²*Photonics Center, Boston University, Boston, Massachusetts 02215, USA*

³*Department of Radiology, Boston University Medical Campus, Boston, Massachusetts 02118, USA*

 (Received 27 July 2022; revised 27 September 2022; accepted 16 November 2022; published 19 December 2022)

Ventilated acoustic insulation currently represents one of the most promising research directions in applied acoustics. With the ongoing development and application of acoustic metamaterials, tremendous progress has been made in this space. In this work, we propose a ventilated acoustic insulator based on a labyrinthine metamaterial, a design that consists of a peripheral, circumferential labyrinthine region and a central ventilated, open region. Herein, we demonstrate the potential for this design to yield high-performance wide-band acoustic insulation, a performance metric currently lacking in this class of acoustic silencers, in combination with ventilation. The silencing effect of the labyrinthine acoustic insulator is theoretically and experimentally verified in the frequency range from 1025 to 2000 Hz. Our reported design establishes the foundation for the development of increasingly broadband ventilated acoustic insulators.

DOI: [10.1103/PhysRevApplied.18.064057](https://doi.org/10.1103/PhysRevApplied.18.064057)

I. INTRODUCTION

Sound insulation represents a major research focus in applied acoustics. Conventionally, sound insulation is achieved using porous sound-absorbing materials or hard, sound-reflecting materials. Though broadband acoustic attenuation may be obtained, it remains challenging to simultaneously realize sound insulation in the low-frequency regime while maintaining ventilation [1].

Acoustic metamaterials (AMMs) [2–13], a type of artificial material consisting of unit cells at the subwavelength scale, offer the capacity to yield unconventional effective properties. Over the past two decades, AMMs have flourished in various applications, allowing us to manipulate acoustic waves in unprecedented ways [11,13–19]. AMMs were initially created for acoustic insulation applications via locally resonant unit cells [14]. Utilizing the principle that locally resonant structural units can exhibit effective negative elastic constants, a unit made of a hard density core coated with high elasticity material realizes exponential acoustic attenuation at 400 Hz. Since then, numerous AMM designs featuring various architectures have been applied to acoustic insulation, including phononic crystals [15,16,20], Helmholtz resonators [21–23], and membrane-type metamaterials [8,24–28], among others. These applications of AMMs have been

reported to yield extraordinary acoustic insulation, especially in the low-frequency regime.

Among potential AMM designs, space-coiling metastructures have been reported to achieve high-performance acoustic insulation in combination with efficient ventilation [29–32]. Space-coiling metastructures feature folded acoustic channels at the subwavelength scale. These engineered designs, such as labyrinthine, curved, and helical channels, can efficiently slow down the sound speed to achieve unusual acoustic properties [33–37]. Based on the concept of the Herschel-Quincke tube [38,39] and Fano-like interference [40], a transverse bilayer design based on helical space-coiling metastructures was proposed to enable high-performance sound silencing with a large open area for air passage [41]. However, a limitation of this design is the fact that the acoustic insulation occurs only within a relatively narrow frequency band. Subsequently, a hornlike helical barrier was proposed to mitigate this limitation. By balancing the system's response between the monopolar and dipolar modes, this design successfully blocks acoustic energy in the range of 900 to 1418 Hz [42]. However, given the broadband nature of noise, ongoing efforts are required to further extend the design library of the broadband ventilated acoustic insulators. In this work, we propose a labyrinthine acoustic insulator design, as shown in Fig. 1(a). The central open area allows the passage of air without any hindrance, while the circumferential labyrinthine region enables acoustic silencing. At the resonant states of the circumferential labyrinthine region, a Fano-like interference of multiple modes mediates the destructive interference at different resonant frequencies,

*stephan.anderson@bmc.org

†xinz@bu.edu

‡These authors contributed equally to this work.

leading to significant noise reduction in a broad frequency band. Our reported design provides an efficient solution towards applications seeking simultaneous ventilation and acoustic silencing.

II. RESULTS AND DISCUSSIONS

A. Labyrinthine unit and its effective medium

The mechanism of the acoustic insulation originates from the acoustic properties of labyrinthine metastructures. In order to identify the acoustic insulation effect, the effective medium theory is employed herein to analyze the labyrinthine region from its geometric and theoretical aspects. As illustrated in Fig. 1(b), in the labyrinthine region, thin plates are assembled to coil up space, wherein plates with a thickness w_1 are placed vertically to divide the channel into zigzag subunits, while plates with a thickness w_2 are placed horizontally to form a hard wall. Given that acoustic waves are scalar waves, at a deep subwavelength scale, acoustic waves will propagate along the

folded directions in the absence of a cut-off frequency [34]. The red arrows in Fig. 1(b) illustrate the propagation path of acoustic waves. When acoustic waves propagate along the labyrinthine channels, a higher refractive index is achieved given that the total length of wave path is much longer than the structure's dimension. Given the dimensions noted in Fig. 1(b), the path length is $L = 5.41t$, such that $n_r = 5.41$. Due to the large impedance mismatch between air and the structure's solid plates, the internal plate walls are considered as rigid boundaries. Hence, the relative mass density and bulk modulus can be approximated by [34] $B_r = 1/(1-f) = 1.78$ and $\rho_r = n_r^2 B_r = 52.10$, where f is the filling ratio of the plates. The mass density and the speed of sound in the background medium (air) are $\rho_1 = 1.22 \text{ kg/m}^3$ and $c_1 = 343 \text{ m/s}$, respectively. From the effective medium point of view, the labyrinthine region can be replaced with a uniform effective medium (EM), with the mass density and the speed of sound in this region as follows: $\rho_2 = \rho_1 \rho_r = 63.56 \text{ kg/m}^3$ and $c_2 = c_1/n_r = 63.40 \text{ m/s}$, respectively. The transmission

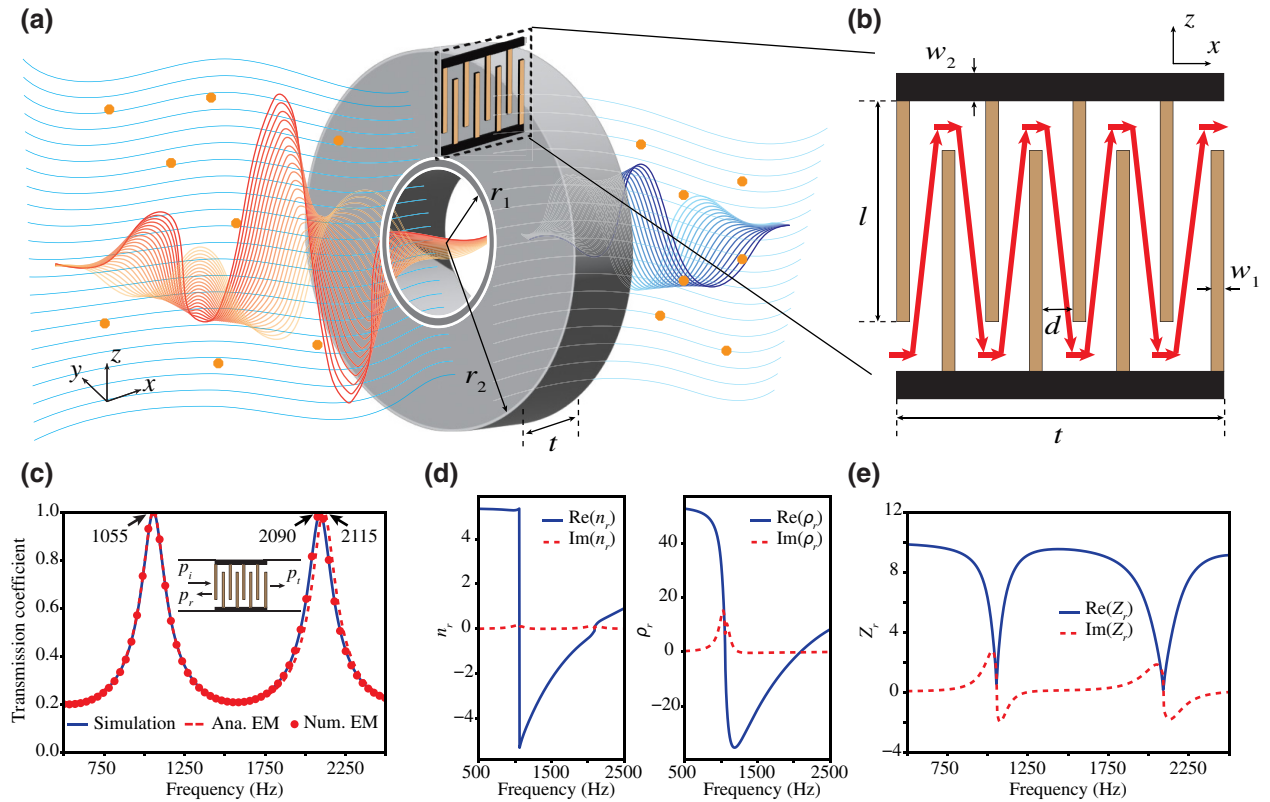


FIG. 1. (a) Schematic diagram of the acoustic insulator design yielding simultaneous ventilation and broadband noise reduction. The profile parameter values are $r_1 = 20 \text{ mm}$, $r_2 = 50 \text{ mm}$, and $t = 30 \text{ mm}$. (b) Cross-section view of the circumferential labyrinthine region; length of vertically placed plates $l = 0.8(r_2 - r_1 - 2w_2) = 20 \text{ mm}$, thickness $w_1 = 1.5 \text{ mm}$, distance between two adjacent plates $d = 2.5 \text{ mm}$, and number of plates $N = 8$; thickness of the horizontally placed plates $w_2 = 2.5 \text{ mm}$. The position of the last plate is aligned with the end of the area. (c) The simulated transmission coefficient of the labyrinthine region (blue line), analytical transmission coefficient (red dashed line), and simulated transmission coefficient (red dots) of the EM. (d) The retrieved relative refractive index n_r and mass density ρ_r as functions of frequency. (e) The retrieved relative acoustic impedance Z_r as a function of frequency.

coefficient of acoustic waves passing from air to the labyrinthine region can be calculated by [43]

$$T = \frac{4Z_1Z_2}{-(Z_1 - Z_2)^2 e^{ik_2t} + (Z_1 + Z_2)^2 e^{-ik_2t}}, \quad (1)$$

where k_2 is the wave number in the EM and $Z_1 = \rho_1 c_1$, $Z_2 = \rho_2 c_2$ are acoustic impedance of air and the EM, respectively. The result is plotted by the red dashed line in Fig. 1(c). It can be observed that the extraordinary acoustic transmission occurs at 1055 and 2115 Hz, which can be attributed to the localized surface resonance as well as the known Fabry-Pérot resonance. At the periodic resonance frequencies, the transmission coefficient achieves 1, indicating an acoustic impedance match between air and the labyrinthine region ($Z_1 = Z_2$). Of note, the above analytical analysis is based on the geometric parameters of the AMM as detailed in Fig. 1(b).

In addition, the transmission coefficient of the labyrinthine region can be numerically obtained by using a full-wave simulation (COMSOL Multiphysics). The insert of Fig. 1(c) illustrates the two-dimensional simulation setup that plane-wave boundaries are set at the inlet and outlet of the waveguide, with the plane wave incident from the left side. The simulated transmission coefficient is plotted by the blue solid line in Fig. 1(c). Despite the fact that there is a slight divergence at high frequencies, there is a relatively high degree of consistency between the analytical result of the EM and simulated result of the real unit in the low-frequency regime. Meanwhile, the effective properties can be verified utilizing the known Fabry-Pérot resonance modes [37]:

$$n_r = c_1/2\Lambda t, \quad (2)$$

$$\rho_r = \frac{n_r}{\sqrt{T_{\min}}} + n_r \sqrt{\frac{1}{T_{\min}} - 1}, \quad (3)$$

where Λ is the first resonance frequency of the Fabry-Pérot resonance and T_{\min} is the lowest transmittance of the structure.

Furthermore, we may apply a retrieval method to extract the effective properties from the simulated reflection and transmission coefficients for a more comprehensive understanding of this labyrinthine region [44]. The effective properties are calculated by

$$n_r = \frac{\pm \cos^{-1} \left(\frac{1}{2T} [1 - (R^2 - T^2)] \right)}{k_1 t} + \frac{2\pi m}{k_1 t}, \quad (4)$$

$$Z_r = \pm \sqrt{\frac{(1 + R)^2 - T^2}{(1 - R)^2 - T^2}}, \quad (5)$$

where k_1 is the wave number in air, m is the branch number, R and T are the simulated reflection and transmission

coefficient, respectively. The retrieved effective properties are plotted in Figs. 1(d) and 1(e). It can be seen that, at the long-wavelength limit, n_r and ρ_r are constants and consistent with previous estimation. As frequency increases, n_r and ρ_r decrease dramatically. Correspondingly, the relative acoustic impedance [$Z_r = \rho_r/n_r$, as shown in Fig. 1(e)], which controls the amplitude of reflection and transmission coefficient, has two minimum values over the frequency spectrum. At these two frequencies, the real part of Z_r approximates 1, indicating an impedance matching at the interface. To validate the retrieved parameters, we use n_r and ρ_r in Fig. 1(d) to simulate a homogeneous slab with the same thickness t . The resulting transmission coefficient is plotted by the red dots in Fig. 1(c) and agrees perfectly with simulation of the real unit.

B. Labyrinthine acoustic insulator

By controlling the effective properties of the labyrinthine metamaterial, we may achieve broadband sound insulation with an open geometry, as shown in Fig. 1(a). In order to understand the physical mechanism behind this insulator design, we consider the geometry as a transverse double-layer structure. The configuration of transverse double-layer structure induces a Fano-like resonance due to the mode interference. The Fano-like interference is characterized by an asymmetric shape in resonance mode, which results from the combination of continuous and discrete states [40]. Given that the peaks in the transmission spectra of the labyrinthine region correspond to different orders of Fabry-Pérot resonant modes, the labyrinthine acoustic insulator design satisfies the requirement of the Fano-like interference. The central open area supports the continuous state while the circumferential labyrinthine region supports the resonant state.

Full-wave simulation is performed on the insulator to verify the soundproofing effect. In the three-dimensional simulation model, the insulator is placed in a cylindrical waveguide and all walls are considered as acoustically rigid. The inlet and outlet boundaries of the waveguide are set with port boundary conditions, while the plane wave with a pressure amplitude of 1 Pa is normally incident from one side. Subsequently, the transmission coefficient is evaluated based on the scattering matrix. The results are plotted in Fig. 2(a). The blue solid line represents the situation when $d = 2.5$ mm, the transmission coefficient decreases dramatically from 1025 Hz, reaches complete acoustic blocking at 1200 Hz, and then rebounds to 0.14 before dropping again to meet another complete acoustic blocking frequency at 1870 Hz. Finally, transmission fully recovers to 1 at 2080 Hz. Ultimately, this design achieves acoustic attenuation that blocks approximately 98% of the incident sound energy in the range of 1025 to 2080 Hz. At 1025 Hz, the acoustic wavelength $\lambda = 334$ mm is 11.1 times larger than the insulator's thickness $t = 30$ mm, such

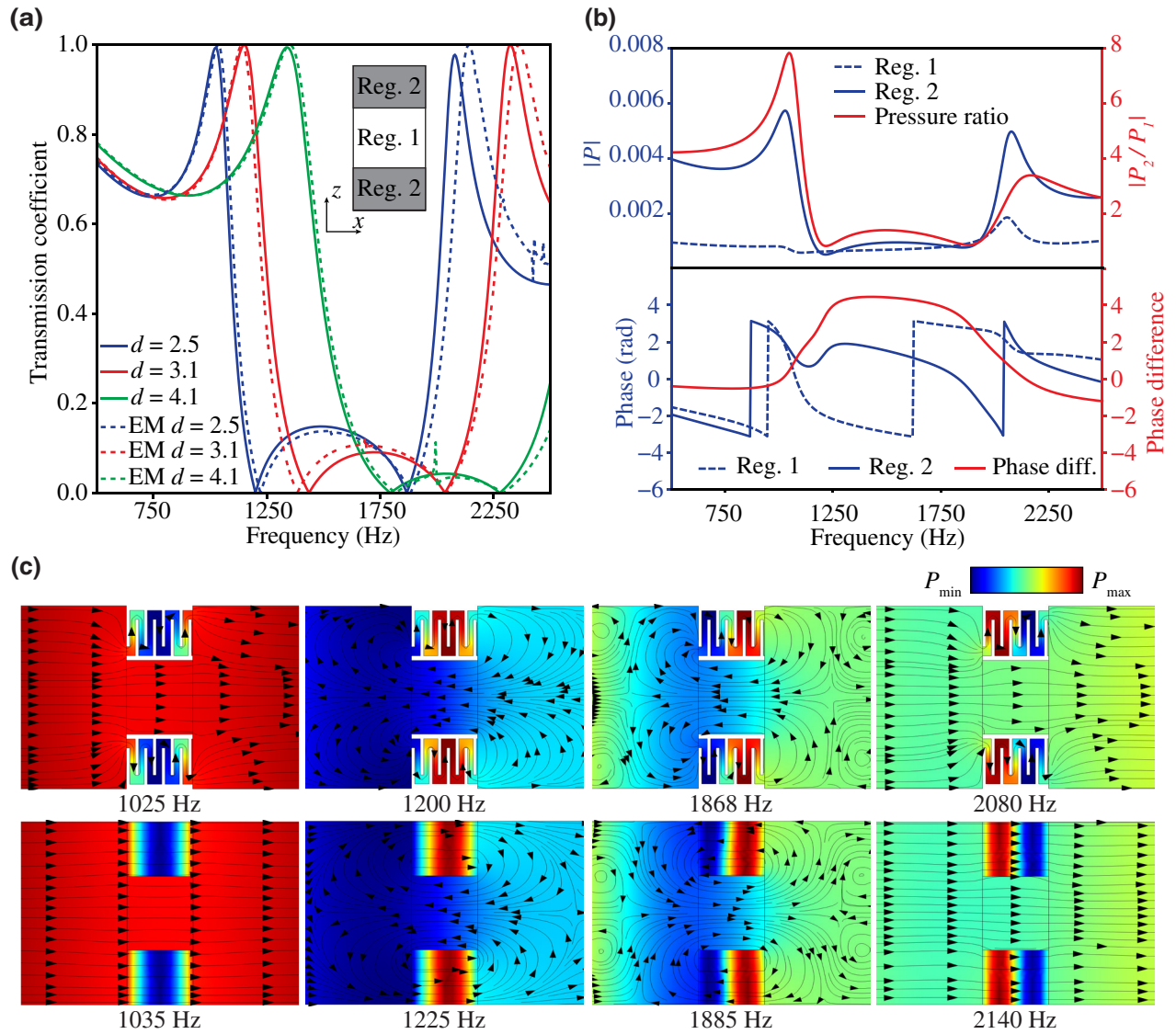


FIG. 2. (a) The simulated transmission coefficient of the labyrinthine acoustic insulator; the solid lines indicate the transmission coefficient of unit cell changing d from 2.5 to 3.1 and 4.1 mm, the dashed lines represent the corresponding effective model. (b) When $d = 2.5$ mm, the pressure amplitudes and phase shift of acoustic waves transmitted through region 1, region 2. (c) Acoustic pressure distribution of the labyrinthine acoustic insulator at various frequencies. Top row corresponds to the real structure, and the bottom row corresponds to results when the labyrinthine region is considered as an effective, homogeneous material.

that the insulator is operating on a deep subwavelength scale. Furthermore, the asymmetric profile of the transmission spectrum around 1025 and 2080 Hz suggests the existence of the Fano-like interference.

The main feature of the Fano-like interference is the constructive and destructive interference resulting from the interaction between scattering waves [45]. Whether these interaction effects are constructive or destructive is determined by the phase and amplitude of acoustic waves propagating through these two regions. To characterize the interference, the pressure distribution and phase shift of the transmitted acoustic waves through the open area and the circumferential labyrinthine region are shown in

Fig. 2(b). For the sake of clarity, we define the central open area as region 1 and the circumferential labyrinthine region as region 2. At peak transmission frequencies of 1025 and 2080 Hz, the phase difference between region 1 and region 2 is 0.12 and 0.58 rad, indicating a dominant constructive interference between these two regions. While at the dip frequencies of 1200 and 1870 Hz, the phase difference is 3.13 and -3.16 rad, respectively. Thus, the interaction of transmitted waves results in destructive interference. Also, as the pressure amplitude of acoustic waves transmitting from region 1 and region 2 are also close to 1, a complete destructive interference is achieved.

In addition to the illustrations of phase and amplitude as functions of frequency, Fig. 2(c) demonstrates the simulated acoustic pressure distribution field and acoustic intensity streamlines of the insulator and its effective medium in a cross-section view. Of note, the effective parameters of EM are retrieved analytically based on geometry. For the real model, at the transmission dip frequencies of 1200 and 1870 Hz, there is a significant drop in the pressure field strength at the front and rear surface of the insulator, with the streamlines showing strong coupling effects between region 1 and region 2. These findings all confirm the existence of the destructive interaction, with the acoustic waves successfully blocked at these frequencies. In contrast, at the two peak frequencies 1025 and 2080 Hz, the field strength distribution remains uniform, with barely any interaction existing and a resultant complete acoustic transmission. Since the analytical EM model is shifted in the transmission spectra compared to the real model, the selected frequency points are changed to 1035, 1225, 1885, and 2140 Hz. The identical pressure distribution inside the real unit and the EM model suggests that the structure can be regarded as a homogeneous material.

C. Tunability and experimental validation

The previous discussion has sought to highlight the correlation between the geometric parameters and the effective acoustic properties of the labyrinthine structure. It is

known that the soundproofing effect of the insulator is tunable by adjusting the internal channels of the circumferential region. The solid lines in Fig. 2(a) illustrate the principle that the broadband acoustic insulation is tunable by adjusting d value. With d increases from 2.5 to 3.1 and 4.1 mm, the transmission spectra shift to higher frequency. In order to yield a more comprehensive understanding of the effects of geometric parameters on the design’s acoustic performance, parameter sweeps are conducted to determine the acoustic transmission in different insulator configurations. Here, the parameter profile of the insulator is defined as follows: $r_1 = 20$ mm, $r_2 = 50$ mm, $t = 30$ mm, $l = 20$ mm, $w_1 = 1.5$ mm, $w_2 = 2.5$ mm, and $N = 8$. The study results are summarized as colormaps in Fig. 3.

Figure 3(a) illustrates the effect of openness of the central region on acoustic attenuation. When r_1 varies, all other parameters are static except l , as l is defined as a ratio connected to r_1 . A larger r_1 leads to a better ventilation and as r_1 increases, acoustic insulation appears at higher frequencies. By trading off a degree of ventilation efficiency, a broader frequency band of acoustic insulation can be achieved at a lower frequency regime. In order to guarantee airflow efficiency and sufficient acoustic energy mitigation, the radius of the open area is set as 20 mm. Furthermore, to analyze the impact of l independently, the value of l is varied through adjusting the ratio in the definition, keeping all other parameters fixed. As shown in

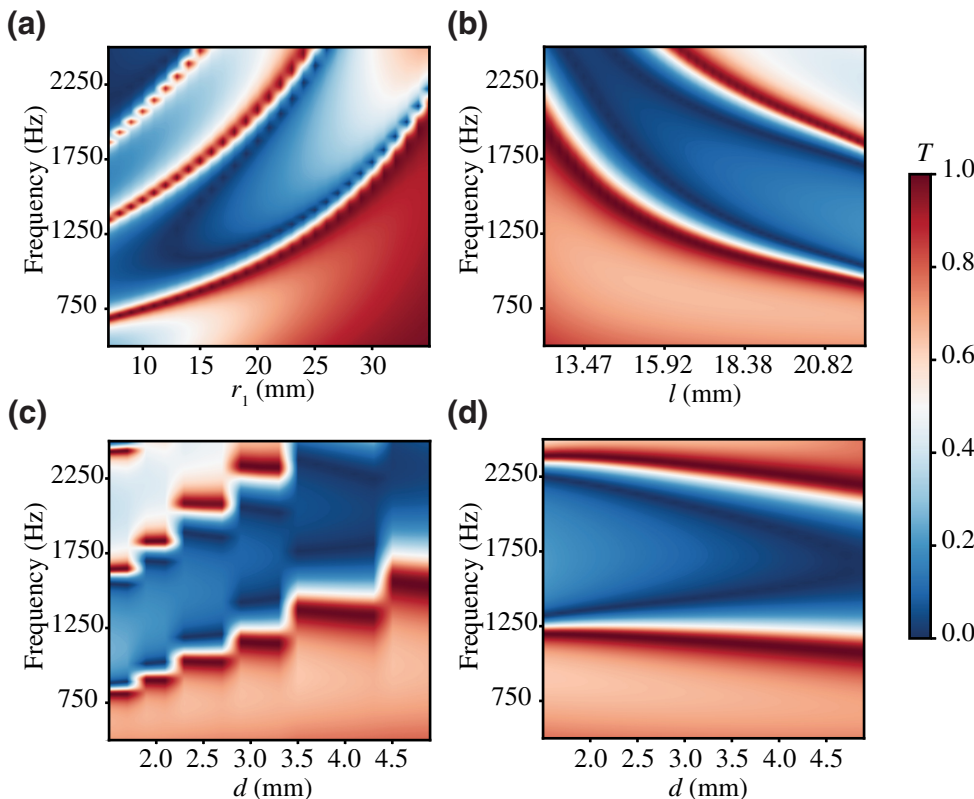


FIG. 3. The transmission coefficient as functions of frequency and geometric parameters. (a) Radius of the central orifice r_1 . (b) Length of the vertically placed plates l . (c) Distance between two adjacent plates d for fixed structure thickness t . (d) Distance between two adjacent plates d for various structure thickness t .

Fig. 3(b), the resonant frequency redshifts as l increases. The total length of wave path in the circumferential region becomes longer for larger values of l , leading to a larger relative refractive index and effective mass density. Considering that the distance between adjacent plates in the labyrinthine metamaterial (d) has the most direct impact on the wave path, we investigate the effects of d in two cases. Figure 3(c) illustrates the case in which the insulator thickness t is fixed. It can be seen that, when d increases, the acoustic insulating effect appears at higher frequencies and the bandwidth also increases. The colormap here shows a stepped manner distribution since the number of the plates is integer and may be various in a discrete fashion. In contrast, when the thickness of the structure t is no longer fixed but changes with the d (keeping the number of plates the same), the operating frequencies are barely shift, as shown in Fig. 3(d). From the above results, we can conclude that any parameter changes leading to the increase of n_r will cause the sound insulation to appear at lower frequencies, and vice versa.

Next, the soundproofing effect of the labyrinthine acoustic insulator is experimentally verified by an impedance tube setup (100 mm B&K 4206-T large impedance tube), as shown in Fig. 4(a). A sample of the designed labyrinthine insulator is fabricated using the fused deposition modeling (FDM) printing technique, as shown in Fig. 4(b). Notably, four cylinder-shaped supports are used to attach the inner part of the labyrinthine plates to the outer frame of the structure, which can be visualized in the rightward aspect of Fig. 4(b). Considering their small dimensions, the impact of these structural supports on the acoustic propagation performance of the overall structure is negligible. In the experiment, the sample is fixed snugly in the central sample holder, and four microphones are placed in the front and rear waveguides to determine the acoustic response of the sample. The measured transmission loss of the sample is indicated as the red triangles in Fig. 4(c). In parallel, the transmission loss of the sample is simulated through frequency-domain analysis. To calculate the acoustic attenuation effect through the sample, the proposed structure is placed in the center of a cylinder waveguide of the same diameter. The front and rear boundaries of the waveguide are set as port boundaries. Considering the high impedance mismatch between the walls and air, all walls are set as acoustically rigid. Next, the simulated transmission loss of the sample is plotted as the blue line in Fig. 4(c). In addition, the acoustic response of this insulator can be theoretically calculated using Green's function (see details in Supplemental Material [46]). For comparison, the transmission loss of a form of identical dimensions (diameter = 100 mm, thickness = 30 mm) but without a central orifice, is measured as the gray dashed line in Fig. 4(c). In Fig. 4(c), the measured transmission loss has two distinct peaks appearing at 1224 and 1870 Hz, corresponding to the destructive interference

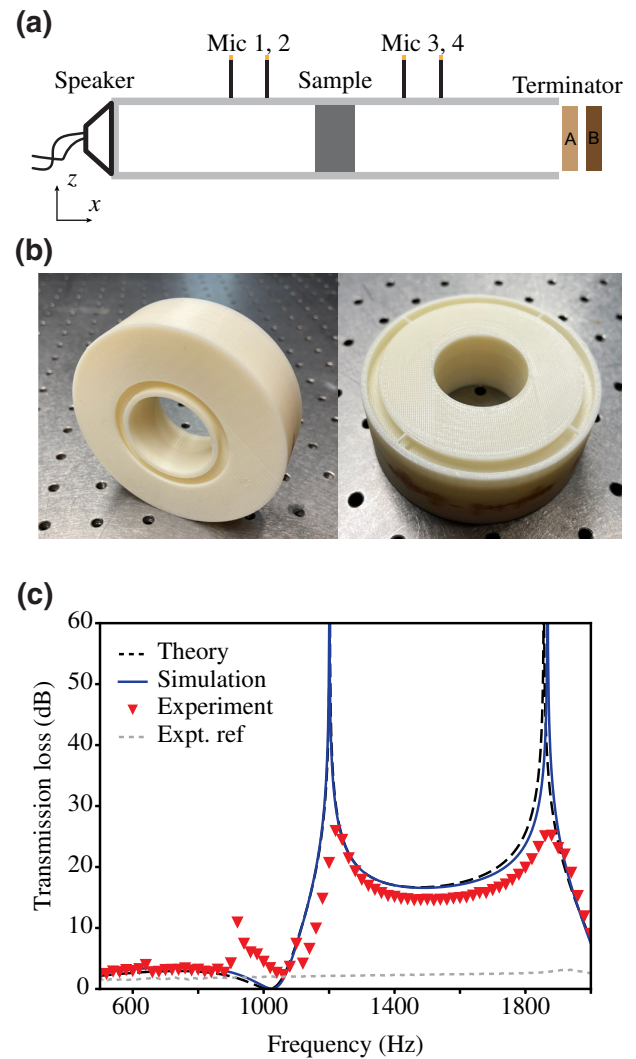


FIG. 4. (a) Schematic diagram of the experimental setup of the impedance tube. (b) The fabricated sample is printed with FDM three-dimensional printing technology in size of $r_1 = 20$ mm, $r_2 = 50$ mm, $t = 30$ mm, $l = 20$ mm, $w_1 = 1.5$ mm, $w_2 = 2.5$ mm, and $N = 8$. (c) Comparison between the transmission loss of theoretical, simulated, and measured result.

frequencies. The result shows a broadband acoustic attenuation from 1060 to 2000 Hz with a transmission loss peak of 26 dB, agreeing well with the simulation and theoretical results.

In practice, noise typically includes diverse incident angles. Thus, we numerically investigate the situation when an incident plane wave propagates at oblique angles. Figure 5 shows that the sound-blocking performance of the proposed structure is insensitive to the incident angles. With a wide-angle range of incidence, the broadband transmission loss is maintained. According to the simulation results, the acoustic attenuation effect becomes even stronger at oblique angles of incidence. This simulated result supports our design's practicality in generalizable

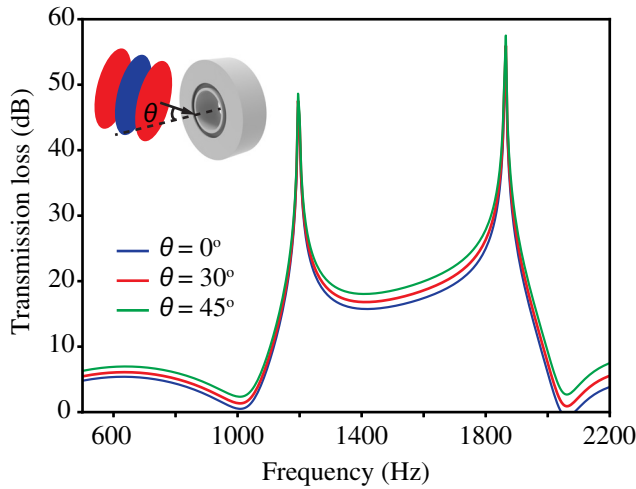


FIG. 5. The simulated transmission loss when the plane wave has incident angles of $\theta = 0^\circ$, $\theta = 30^\circ$, and $\theta = 45^\circ$.

scenarios with acoustic waves impinging from various angles.

Furthermore, measurements are conducted to investigate the ventilation performance of the proposed design. Figure 6(a) is the diagram of the experimental setup, in which an electric fan is placed in the inlet, the sample is placed snugly inside the waveguide, while a digital anemometer is placed at the outlet to record the wind-flow velocity. The ventilation performance is characterized by measuring the wind-flow velocity with and without the sample inside the waveguide. As shown in Fig. 6(b), the measured results and the fitted line are plotted as maroon dots and a solid line, respectively. The linear characteristic of the fitting line supports the conclusion that the effectiveness of wind-flow ventilation approximates 39%, where the effectiveness of ventilation is defined as the wind-velocity ratio between airflow velocities with and without the sample.

Lastly, considering that the presence of airflow in the system would alter the acoustic properties, we also numerically investigate the impact of airflow on the transmission loss of the designed structure. In this model, SST turbulence and linearized Navier-Stokes, frequency domain modules of COMSOL Multiphysics are coupled to determine the transmission-loss performance. The transmission loss is simulated at discrete frequencies for conditions when there is no airflow (Ma as the Mach number, $Ma = 0$) as well as two flow cases ($Ma = 0.01, 0.02$), as shown in Fig. 6(c). When there is no airflow, the soundproofing effect is the same as results obtained in Fig. 4(c). However, in the presence of airflow in the waveguide, due to the high dissipation caused by the grazing flow, transmission loss peaks are reduced significantly while shifting the peak interference towards lower frequencies. Nevertheless, the broadband soundproofing profile remains unchanged,

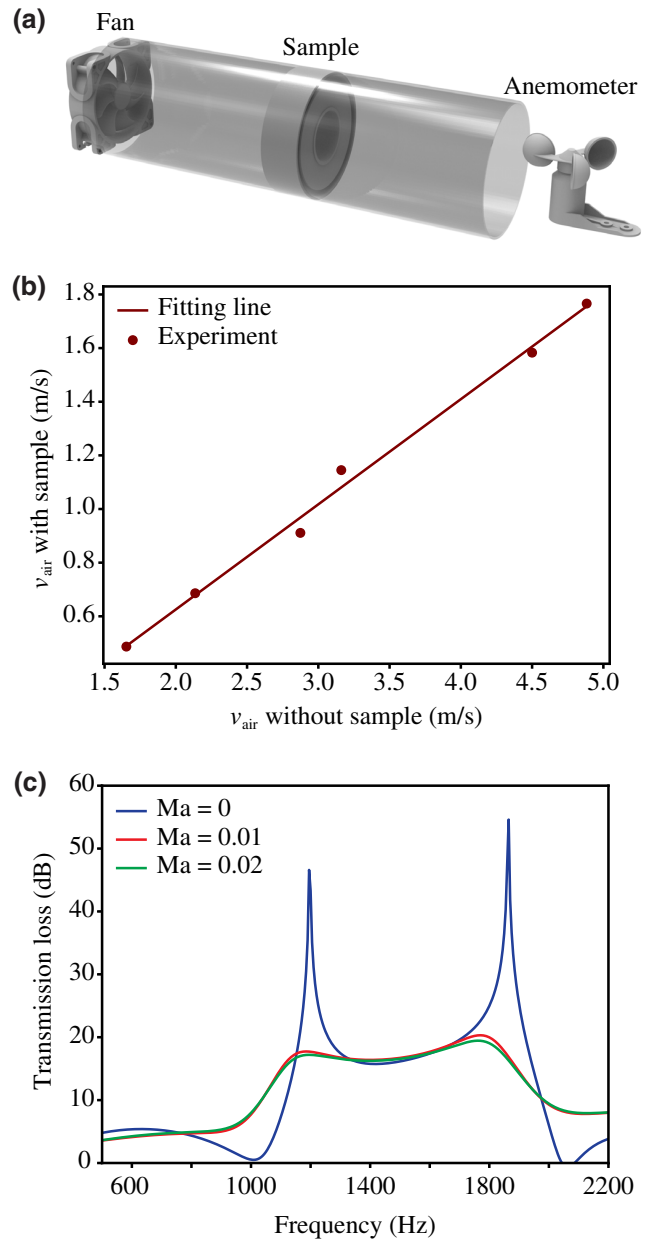


FIG. 6. (a) Schematic diagram of the ventilation characterization setup. (b) The measured airflow velocity with or without sample. The maroon line is the fitting result of the measured results. (c) The simulated transmission loss of the insulator with different airflow speed.

suggesting that this insulator design yields broadband acoustic attenuation in the presence of airflow.

III. CONCLUSION

In conclusion, we numerically and experimentally demonstrate a labyrinthine, or space-coiling, based sound insulator. This design, composed of a circumferential labyrinthine region and a central open area, enables efficient ventilation and broadband soundproofing in the

low-frequency regime. Due to the phase-delay characteristic of the labyrinthine space-coiling structure, the Fano-like interference and the accompanied destructive interaction realize an efficient blocking of incident acoustic energy in the range of 1025 to 2000 Hz with a $1/11\lambda$ thickness. Additionally, adopting the labyrinthine structure endows the unit great tunability in its acoustic insulation performance. Numerical and experimental results successfully verified our design methodology. Our work offers a solution of a broadband acoustic insulator with efficient ventilation.

ACKNOWLEDGMENTS

The authors would like to thank Boston University Photonics Center for funding and technical support.

-
- [1] J. Allard and N. Atalla, *Propagation of sound in porous media: modelling sound absorbing materials 2e* (John Wiley & Sons, 2009).
- [2] S. A. Cummer, B.-I. Popa, D. Schurig, D. R. Smith, J. Pendry, M. Rahm, and A. Starr, Scattering Theory Derivation of a 3D Acoustic Cloaking Shell, *Phys. Rev. Lett.* **100**, 024301 (2008).
- [3] J. Li and J. B. Pendry, Hiding Under the Carpet: A New Strategy for Cloaking, *Phys. Rev. Lett.* **101**, 203901 (2008).
- [4] M. Farhat, S. Guenneau, and S. Enoch, Ultrabroadband Elastic Cloaking in Thin Plates, *Phys. Rev. Lett.* **103**, 024301 (2009).
- [5] B.-I. Popa, L. Zigoneanu, and S. A. Cummer, Experimental Acoustic Ground Cloak in Air, *Phys. Rev. Lett.* **106**, 253901 (2011).
- [6] S. Zhang, C. Xia, and N. Fang, Broadband Acoustic Cloak for Ultrasound Waves, *Phys. Rev. Lett.* **106**, 024301 (2011).
- [7] Y. Xie, W. Wang, H. Chen, A. Konneker, B.-I. Popa, and S. A. Cummer, Wavefront modulation and subwavelength diffractive acoustics with an acoustic metasurface, *Nat. Commun.* **5**, 1 (2014).
- [8] G. Ma, M. Yang, S. Xiao, Z. Yang, and P. Sheng, Acoustic metasurface with hybrid resonances, *Nat. Mater.* **13**, 873 (2014).
- [9] J. Li, L. Fok, X. Yin, G. Bartal, and X. Zhang, Experimental demonstration of an acoustic magnifying hyperlens, *Nat. Mater.* **8**, 931 (2009).
- [10] J. Zhu, J. Christensen, J. Jung, L. Martin-Moreno, X. Yin, L. Fok, X. Zhang, and F. Garcia-Vidal, A holey-structured metamaterial for acoustic deep-subwavelength imaging, *Nat. Phys.* **7**, 52 (2011).
- [11] N. Kaina, F. Lemoult, M. Fink, and G. Lerosey, Negative refractive index and acoustic superlens from multiple scattering in single negative metamaterials, *Nature* **525**, 77 (2015).
- [12] T. Brunet, A. Merlin, B. Mascaro, K. Zimny, J. Leng, O. Poncelet, C. Aristégui, and O. Mondain-Monval, Soft 3D acoustic metamaterial with negative index, *Nat. Mater.* **14**, 384 (2015).
- [13] S. H. Lee, C. M. Park, Y. M. Seo, Z. G. Wang, and C. K. Kim, Composite Acoustic Medium with Simultaneously Negative Density and Modulus, *Phys. Rev. Lett.* **104**, 054301 (2010).
- [14] Z. Liu, X. Zhang, Y. Mao, Y. Zhu, Z. Yang, C. T. Chan, and P. Sheng, Locally resonant sonic materials, *Science* **289**, 1734 (2000).
- [15] M. S. Kushwaha, P. Halevi, L. Dobrzynski, and B. Djafari-Rouhani, Acoustic Band Structure of Periodic Elastic Composites, *Phys. Rev. Lett.* **71**, 2022 (1993).
- [16] R. Martínez-Sala, J. Sancho, J. V. Sánchez, V. Gómez, J. Llinares, and F. Meseguer, Sound attenuation by sculpture, *Nature* **378**, 241 (1995).
- [17] C. Goffaux, J. Sánchez-Dehesa, A. Levy-Yeyati, P. Lambin, A. Khelif, J. O. Vasseur, and B. Djafari-Rouhani, Evidence of Fano-like Interference Phenomena in Locally Resonant Materials, *Phys. Rev. Lett.* **88**, 225502 (2002).
- [18] H. Huang, C. Sun, and G. Huang, On the negative effective mass density in acoustic metamaterials, *Int. J. Eng. Sci.* **47**, 610 (2009).
- [19] J. Li and C. T. Chan, Double-negative acoustic metamaterial, *Phys. Rev. E* **70**, 055602(R) (2004).
- [20] F. Lemoult, N. Kaina, M. Fink, and G. Lerosey, Wave propagation control at the deep subwavelength scale in metamaterials, *Nat. Phys.* **9**, 55 (2013).
- [21] N. Fang, D. Xi, J. Xu, M. Ambati, W. Srituravanich, C. Sun, and X. Zhang, Ultrasonic metamaterials with negative modulus, *Nat. Mater.* **5**, 452 (2006).
- [22] X. Cai, Q. Guo, G. Hu, and J. Yang, Ultrathin low-frequency sound absorbing panels based on coplanar spiral tubes or coplanar Helmholtz resonators, *Appl. Phys. Lett.* **105**, 121901 (2014).
- [23] R. Dong, D. Mao, X. Wang, and Y. Li, Ultrabroadband Acoustic Ventilation Barriers via Hybrid-Functional Metasurfaces, *Phys. Rev. Appl.* **15**, 024044 (2021).
- [24] Z. Yang, J. Mei, M. Yang, N. H. Chan, and P. Sheng, Membrane-type Acoustic Metamaterial with Negative Dynamic Mass, *Phys. Rev. Lett.* **101**, 204301 (2008).
- [25] Z. Yang, H. Dai, N. Chan, G. Ma, and P. Sheng, Acoustic metamaterial panels for sound attenuation in the 50–1000 Hz regime, *Appl. Phys. Lett.* **96**, 041906 (2010).
- [26] J. Mei, G. Ma, M. Yang, Z. Yang, W. Wen, and P. Sheng, Dark acoustic metamaterials as super absorbers for low-frequency sound, *Nat. Commun.* **3**, 1 (2012).
- [27] S. Xiao, G. Ma, Y. Li, Z. Yang, and P. Sheng, Active control of membrane-type acoustic metamaterial by electric field, *Appl. Phys. Lett.* **106**, 091904 (2015).
- [28] M. Yang, G. Ma, Z. Yang, and P. Sheng, Coupled Membranes with Doubly Negative Mass Density and Bulk Modulus, *Phys. Rev. Lett.* **110**, 134301 (2013).
- [29] H.-l. Zhang, Y.-f. Zhu, B. Liang, J. Yang, J. Yang, and J.-c. Cheng, Omnidirectional ventilated acoustic barrier, *Appl. Phys. Lett.* **111**, 203502 (2017).
- [30] J. Yang, J. S. Lee, H. R. Lee, Y. J. Kang, and Y. Y. Kim, Slow-wave metamaterial open panels for efficient reduction of low-frequency sound transmission, *Appl. Phys. Lett.* **112**, 091901 (2018).
- [31] S. Kumar and H. P. Lee, Labyrinthine acoustic metastructures enabling broadband sound absorption and ventilation, *Appl. Phys. Lett.* **116**, 134103 (2020).

- [32] C. Liu, J. Shi, W. Zhao, X. Zhou, C. Ma, R. Peng, M. Wang, Z. H. Hang, X. Liu, and J. Christensen, *et al.*, Three-Dimensional Soundproof Acoustic Metacage, *Phys. Rev. Lett.* **127**, 084301 (2021).
- [33] Y. Li, B. Liang, X. Tao, X.-f. Zhu, X.-y. Zou, and J.-c. Cheng, Acoustic focusing by coiling up space, *Appl. Phys. Lett.* **101**, 233508 (2012).
- [34] Z. Liang and J. Li, Extreme Acoustic Metamaterial by Coiling Up Space, *Phys. Rev. Lett.* **108**, 114301 (2012).
- [35] Y. Li, B. Liang, X.-y. Zou, and J.-c. Cheng, Extraordinary acoustic transmission through ultrathin acoustic metamaterials by coiling up space, *Appl. Phys. Lett.* **103**, 063509 (2013).
- [36] Y. Xie, B.-I. Popa, L. Zigoneanu, and S. A. Cummer, Measurement of a Broadband Negative Index with Space-Coiling Acoustic Metamaterials, *Phys. Rev. Lett.* **110**, 175501 (2013).
- [37] X. Zhu, K. Li, P. Zhang, J. Zhu, J. Zhang, C. Tian, and S. Liu, Implementation of dispersion-free slow acoustic wave propagation and phase engineering with helical-structured metamaterials, *Nat. Commun.* **7**, 1 (2016).
- [38] J. F. Herschel, Lxiii. on the absorption of light by coloured media, viewed in connexion with the undulatory theory, London, Edinburgh, Dublin *Philos. Mag. J. Sci.* **3**, 401 (1833).
- [39] G. Quincke, *Ueber interferenzapparate für schallwellen* (1866).
- [40] U. Fano, Effects of configuration interaction on intensities and phase shifts, *Phys. Rev.* **124**, 1866 (1961).
- [41] R. Ghaffarivardavagh, J. Nikolajczyk, S. Anderson, and X. Zhang, Ultra-open acoustic metamaterial silencer based on Fano-like interference, *Phys. Rev. B* **99**, 024302 (2019).
- [42] M. Sun, X. Fang, D. Mao, X. Wang, and Y. Li, Broadband Acoustic Ventilation Barriers, *Phys. Rev. Appl.* **13**, 044028 (2020).
- [43] L. Brekhovskikh, *Waves in Layered Media* (Elsevier, New York, 2012), Vol. 16.
- [44] V. Fokin, M. Ambati, C. Sun, and X. Zhang, Method for retrieving effective properties of locally resonant acoustic metamaterials, *Phys. Rev. B* **76**, 144302 (2007).
- [45] A. E. Miroshnichenko, S. Flach, and Y. S. Kivshar, Fano resonances in nanoscale structures, *Rev. Mod. Phys.* **82**, 2257 (2010).
- [46] See Supplemental Material at <http://link.aps.org/supplemental/10.1103/PhysRevApplied.18.064057> for detailed discussions of theoretical analysis of the broadband labyrinthine acoustic insulator, experimental setup, and the impact of airflow rate on the background acoustic pressure.
- [47] H. Nguyen, Q. Wu, H. Chen, J. Chen, Y. Yu, S. Tracy, and G. Huang, A Fano-based acoustic metamaterial for ultra-broadband sound barriers, *Proc. R. Soc. A* **477**, 20210024 (2021).
- [48] ASTM: E2611-09: Standard test method for measurement of normal incidence sound transmission of acoustical materials based on the transfer matrix method, ASTM International, West Conshohocken, PA, USA (2009).